

## Article

# Two Consecutive Negative Electrocaloric Peaks in <001>-Oriented PMN-30PT Single Crystals

Yu Zhang <sup>1</sup>, Weiping Gong <sup>2</sup> , Zhen Li <sup>3</sup>, Jianting Li <sup>1,4,\*</sup>, Changyu Li <sup>1,4</sup>, Jun Chen <sup>1,4</sup>, Yaodong Yang <sup>1,4</sup> , Yang Bai <sup>5</sup> and Wei-Feng Rao <sup>1,4</sup>

<sup>1</sup> School of Mechanical Engineering, Qilu University of Technology (Shandong Academy of Sciences), Jinan 250353, China; z1252790385@163.com (Y.Z.); 202201020028@stu.qlu.edu.cn (C.L.); chenjun@qlu.edu.cn (J.C.); yaodongy@qlu.edu.cn (Y.Y.); wfrao@qlu.edu.cn (W.-F.R.)

<sup>2</sup> Guangdong Provincial Key Laboratory of Electronic Functional Materials and Devices, Huizhou University, Huizhou 516001, China; gwp@hzu.edu.cn

<sup>3</sup> Kyiv College, Qilu University of Technology (Shandong Academy of Sciences), Jinan 250353, China; 202181020041@stu.qlu.edu.cn

<sup>4</sup> Shandong Institute of Mechanical Design and Research, Jinan 250353, China

<sup>5</sup> Beijing Advanced Innovation Center for Materials Genome Engineering, University of Science and Technology Beijing, Beijing 100083, China; baiy@mater.ustb.edu.cn

\* Correspondence: lijianting@qlu.edu.cn

**Abstract:** The versatile electrocaloric (EC) behaviors of the  $(1-x)\text{Pb}(\text{Mg}_{1/3}\text{Nb}_{2/3})\text{O}_{3-x}\text{PT}$  (PMN-100xPT) single crystal are closely related to the multiple phase transitions under the multiple fields of electric field and temperature. In this work, the EC effect of <001>-oriented PMN-30PT single crystals with chemical composition at morphotropic phase boundary has been studied during the phase transformation process from the ferroelectric rhombohedral (*R*) phase to the tetragonal (*T*) phase. Two consecutive negative EC peaks have been achieved for the first time. Based on the projection of the EC effect in the electric field-temperature phase diagram, the relationship between the EC behaviors and the phase transitions is further established. It was found that the monoclinic (*M*) phase actually existed during the transformation from the *R* phase to the *T* phase, and the related *R*-*M* phase transition and *M*-*T* phase transition could both induce negative EC peaks. Under the electric field of  $E = 10 \text{ kV/cm}$ , the first negative EC peaks induced by the *R*-*M* phase transition is at  $57^\circ\text{C}$  with  $\Delta T_{\text{max}} = -0.11 \text{ K}$ . And the *M*-*T* phase transition can produce a higher negative EC peak, and its value can reach  $-0.22 \text{ K}$  at  $68^\circ\text{C}$ . Based on thermodynamic calculations, the relationship between the entropy change in different phase transitions and the EC behaviors has been further elucidated. The negative EC effect originates from the structural entropy increase in the electric field-induced phase transition process. This work not only advances the research on the electrical properties of relaxor ferroelectric single crystals but also provides a new insight into high-performance ferroelectric materials design.



check for updates

**Citation:** Zhang, Y.; Gong, W.; Li, Z.; Li, J.; Li, C.; Chen, J.; Yang, Y.; Bai, Y.; Rao, W.-F. Two Consecutive Negative Electrocaloric Peaks in <001>-Oriented PMN-30PT Single Crystals. *Crystals* **2024**, *14*, 458. <https://doi.org/10.3390/cryst14050458>

Academic Editor: Jagdish K. Vij

Received: 11 April 2024

Revised: 27 April 2024

Accepted: 9 May 2024

Published: 12 May 2024

**Keywords:** electrocaloric effect; negative electrocaloric effect; phase transitions; phase diagram



**Copyright:** © 2024 by the authors. Licensee MDPI, Basel, Switzerland. This article is an open access article distributed under the terms and conditions of the Creative Commons Attribution (CC BY) license (<https://creativecommons.org/licenses/by/4.0/>).

## 1. Introduction

As the environmental crisis brought about by fluorine-containing greenhouse gases becomes more and more serious, a new and frontier refrigeration technology that is environmentally friendly is extremely expected to replace conventional mechanical vapor-compression refrigeration [1]. Among the many green refrigeration technologies, ferroelectric refrigeration based on the electrocaloric (EC) effect is regarded as the most promising alternative for the compressor due to its unparalleled advantages, such as environmental friendliness, easy miniaturization, easy modulation, high conversion efficiency, low cost, and zero emission [2]. The EC effect is the adiabatic temperature change ( $\Delta T$ ) or the isothermal entropy change ( $\Delta S$ ) resulting from the application or withdrawal of an electric field ( $\Delta E$ ) in polarizable materials.

The EC effect was first observed in the 1930s by Kobeko and Kurtschoatov in Rochelle Salt, but the small temperature difference did not receive widespread attention [3]. In 2006, Mischenko et al. achieved a giant EC effect with  $\Delta T = 12$  K near the ferroelectric–paraelectric phase transition in  $\text{PbZr}_{0.95}\text{Ti}_{0.05}\text{O}_3$  thin films under the excitation of an ultrahigh electric field with  $\Delta E = 480$  kV/cm [4]. In 2008, Neese et al. also reported a giant EC effect with  $\Delta T = 12$  K in P(VDF-TrFE)-based ferroelectric polymer thin films under  $\Delta E = 3000$  kV/cm [5]. These two works demonstrate the enormous application value of ferroelectric refrigeration, which sparked a research boom in the EC field. Since then, significant progress has been made in high-performance EC materials and ferroelectric refrigeration devices [6–11]. For example, Qian et al. prepared a polarized high entropy polymer and achieved a significant giant EC effect with  $\Delta S = 37.5$  J kg<sup>-1</sup> K<sup>-1</sup> and  $\Delta T = 7.5$  K [11]. In 2023, Li et al. developed a ferroelectric refrigeration device that could generate a temperature difference of 20 kelvin or 4.2 watts of cooling power [9]. These excellent works have greatly promoted the practical application of ferroelectric refrigeration technology.

According to the temperature response of the ferroelectric material under an external electric field, the EC effect can be further divided into positive EC effect and negative EC effect; some jobs also refer to it as abnormal EC effect or inverse EC effect [12,13]. In the normal case, the temperature of polar materials will increase ( $\Delta T > 0$ ) when an electric field is applied, i.e., positive EC effect. Both experiments and theories prove that the ultrahigh positive EC peaks usually occur at the ferroelectric–paraelectric phase transitions, while the negative EC effect indicates that the temperature of the material decreases ( $\Delta T < 0$ ) when an electric field is applied. Materials with a positive EC effect release heat into the environment when an external electric field is applied and absorb heat from the environment when the electric field is removed, while the heat exchange process for materials with negative EC effects is the opposite. In 2011, the negative EC effect was first reported in bismuth sodium titanate-based ferroelectric materials [12], which enriched the EC territory and physical mechanisms. Up to now, the negative EC effect has been observed only in a very small amount of materials, for example, the antiferroelectric materials [14,15], specially oriented ferroelectric single crystal materials [13,16], and some materials with high rectangular polarization loops [17,18]. Compared to the positive EC effect, the negative EC effect is difficult to obtain, mainly because it is restricted by the conditions of the external field, such as the temperature, electric field, and stress [13–21]. Recently, negative EC effects and materials have attracted increasing attention because they could provide a new path to improve the ferroelectric refrigeration performance by combining the positive EC effects in a valid cooling cycle [22–24].

The  $(1-x)\text{Pb}(\text{Mg}_{1/3}\text{Nb}_{2/3})\text{O}_3-x\text{PbTiO}_3$  (PMN-100xPT) single crystal is considered to be a promising material for efficient solid-state cooling devices because of its coexistence of positive and negative ECE, especially after a practical dual-refrigeration cycle combining the positive and negative EC effect was proposed [22]. It demonstrates that the positive and negative EC effects in PMN-100xPT single crystals with chemical composition at morphotropic phase boundary (MPB) are attributed to their complex electric-field-induced phase transition behavior. However, there is still controversy over the phase transition process of PMN-100xPT single crystals at MPB. Some studies believe that the crystal transforms from the initial ferroelectric rhombohedral (*R*) phase to the tetragonal (*T*) phase and becomes the paraelectric cubic (*C*) phase above the Curie temperature under the multiple fields of electric field and temperature [16]. Under adiabatic conditions, the phase transition of the low-temperature *R* phase to the high-temperature *T* phase induced by a non-collinear electric field can produce a negative EC peak [25], while the *T*-*C* phase transition can produce a positive EC peak. However, some researchers who focus on the piezoelectric properties of the relaxor ferroelectric single crystal have found that there was an intermediate monoclinic (*M*) phase during the *R*-*T* phase transition [26–29]. If this is the case, the traditionally considered *R*-*T* phase transition process will be divided into three parts, namely, *R*-*M* phase transition, single ferroelectric *M* phase transition, and *M*-*T* phase transition. In 2017, Wu and Cohen found a negative EC peak induced by *R*-*M<sub>A</sub>* phase

transition via classical molecular dynamics [30]. But for the *M-T* phase transition, there was a positive EC peak. However, the direct method results of the EC effect of PMN-30PT single crystals showed that the negative EC peak was induced by the *M-T* phase transition, which has a higher energy barrier, while there is no negative EC peak near the *R-M* phase transition [31]. As for why these two phase transitions (*R-M* and *M-T*) only produce one negative EC peak, the reasons are still unclear. Therefore, clarifying the physical mechanism behind the behavior of the negative EC effect is of great significance for the study of EC materials and the design of high-efficiency refrigeration cycles.

In this work, we explored the EC behaviors more delicately in <001>-oriented PMN-30PT single crystals under the multiple fields of electric field and temperature field and discovered the continuous negative EC peaks induced by the *R-M* and *M-T* phase transitions for the first time in this experiment. An electric field-temperature (*E-T*) phase diagram was drawn based on the changes in the unipolar polarization. Moreover, through phenomenological calculations and analysis, the close relationships between the negative EC peaks and the phase transition are further established.

## 2. Experimental Procedure

### 2.1. Experimental Methods

The 0.7Pb(Mg<sub>1/3</sub>Nb<sub>2/3</sub>)O<sub>3</sub>-0.3PbTiO<sub>3</sub> (PMN-30PT) single crystals, which were grown by the Bridgman technique, were commercially purchased from the SICCAS High Technology Corporation company. The PMN-30PT crystals were cut perpendicular to the <001> direction into plates with a size of 5 mm × 5 mm × 1 mm. The crystal samples were polished and coated with electrodes on both sides for subsequent electrical performance testing. The crystals were pre-poled with a DC electric field of *E* = 2 kV/cm at room. The dielectric properties of unpoled and pre-poled crystals were measured by an LCR meter (Keysight E4980A, America) equipped with an automated temperature controller at different frequencies (0.1, 1, 10, and 100 kHz) from room temperature to 250 °C with heating ramp rates of 1 °C/min. The ferroelectric performance was characterized by a ferroelectric analyzer (TF1000, aixACCT). The unipolar polarization–electric field (*P-E*) curves were tested with intervals of 10 °C under an electric field with an intensity of 10 kV/cm and a frequency of 1 Hz. The bipolar *P-E* loops were tested with intervals of 2 °C under the same electric field conditions.

### 2.2. Phenomenological Theoretical Calculations

In order to elucidate the evolution process of crystal structure and related electrical properties, phenomenological theoretical calculations have also been carried out based on the following tenth-order Landau–Devonshire free energy model [32]:

$$G = \alpha_1 J_1 + \alpha_{11} J_1^2 + \alpha_2 J_2 + \alpha_{12} J_1 J_2 + \alpha_{111} J_1^3 + \alpha_3 J_3 + \alpha_{1111} J_1^4 + \alpha_{13} J_1 J_3 + \alpha_{22} J_2^2 + \alpha_{122} J_1 J_2^2 - E_1 P_1 - E_2 P_2 - E_3 P_3 \quad (1)$$

where  $J_1 = P_1^2 + P_2^2 + P_3^2$ ,  $J_2 = P_1^2 P_2^2 + P_1^2 P_3^2 + P_2^2 P_3^2$  and  $J_3 = P_1^2 P_2^2 P_3^2$  are the basis invariants composed of the polarization components  $P_1$ ,  $P_2$ , and  $P_3$ ;  $E_1$ ,  $E_2$ , and  $E_3$  represent the applied electric field strength; the  $\alpha_1$ ,  $\alpha_{11}$ ,  $\alpha_{12}$ ,  $\alpha_{111}$ ,  $\alpha_3$ ,  $\alpha_{1111}$ ,  $\alpha_{13}$ ,  $\alpha_{22}$ , and  $\alpha_{122}$  are the dielectric stiffness coefficients, which are listed in Table 1.

**Table 1.** Values of the dielectric stiffness coefficients of the LGD potential model (1) [32].

Coefficients	Numerical Values	Units
$\alpha_1$	$8.5602 \times 10^4 \times (T-359) - 5.1361 \times 10^7 \times (x - 0.255)$	$C^{-2}m^2N$
$\alpha_2$	$3.6692 \times 10^5 \times (T-359) + 1.8205 \times 10^9 \times (x - 0.255)$	$C^{-4}m^6N$
$\alpha_{11}$	$-7.5298 \times 10^7$	$C^{-4}m^6N$
$\alpha_{111}$	$9.7853 \times 10^8$	$C^{-6}m^{10}N$
$\alpha_{12}$	$-2.3065 \times 10^9$	$C^{-6}m^{10}N$

Table 1. Cont.

Coefficients	Numerical Values	Units
$\alpha_3$	$1 \times 10^6$	$C^{-6}m^{10}N$
$\alpha_{1111}$	$3.7752 \times 10^9$	$C^{-8}m^{14}N$
$\alpha_{22}$	$2.5 \times 10^{10}$	$C^{-8}m^{14}N$
$\alpha_{13}$	$4 \times 10^8$	$C^{-8}m^{14}N$
$\alpha_{122}$	$1 \times 10^9$	$C^{-10}m^{18}N$

### 3. Results and Discussion

#### 3.1. Effect of the Electric Field and the Temperature on Phase Transition

Figure 1a shows the dielectric constant and loss as a function of temperature for the pre-poled <001>-oriented PMN-30PT single crystals. There are three dielectric anomaly peaks at 89 °C, 97 °C, and 128 °C, indicating three phase transitions in the process. The variable temperature X-ray diffraction (XRD) spectrum was tested to investigate the phase transition process. However, the XRD spectrum showed orientation peaks but failed to display crystal structure information, as shown in the illustration in Figure 1a. Figure 1b demonstrated the polarization components ( $P_1$ ,  $P_2$ , and  $P_3$ ) of the PMN-30PT single crystal, which can be determined by solving the equilibrium Equation (1) with  $\partial G/\partial P_i = 0$  ( $i = 1, 2, 3$ ). When the temperature is low, the polarization parameter  $P_1 = P_2 = P_3 > 0$  shows that the single crystal is in a ferroelectric rhombohedral (R) phase. As the temperature increases, the crystal will sequentially transform into monoclinic (M,  $P_1 \neq P_2 \neq P_3$ ), tetragonal (T,  $P_3 > 0, P_1 = P_2 = 0$ ), and cubic (C,  $P_1 = P_2 = P_3 = 0$ ) phases.

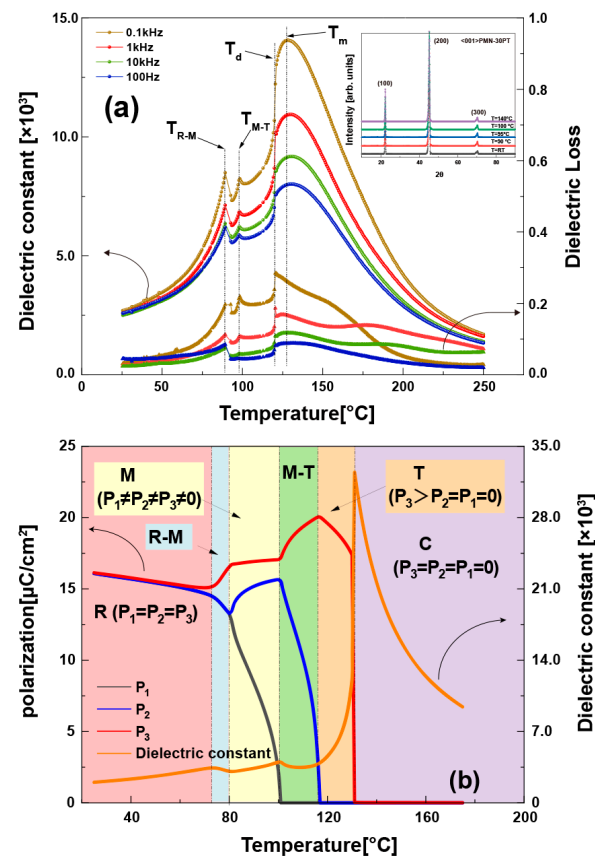


Figure 1. (a) dielectric constant and loss as functions of temperature for the pre-poled <001>-oriented PMN-30PT single crystals; (b) the polarization parameter (black line for  $P_1$ , blue line for  $P_2$  and red line for  $P_3$ ) and dielectric constants (Yellow line) calculated by LGD potential model.

The dielectric constant in Figure 1b was calculated as

$$\chi_{ij} = \left( \frac{\partial^2 G}{\partial P_i \partial P_j} \right)^{-1}, \quad (2)$$

$$\varepsilon_{ij} = \varepsilon_0 + \chi_{ij} \quad (3)$$

where  $\chi_{ij}$  is the component of dielectric susceptibility;  $\varepsilon_{ij}$  is the component of dielectric constants, and  $\varepsilon_0$  is the electric constant:  $8.85 \times 10^{-12} \text{ C}^2/\text{Nm}^2$ . Theoretical calculations and experimental results of pre-poled <001>-oriented PMN-30PT are consistent. The three dielectric anomalies in a dielectric constant curve, from low to high temperature, correspond to the *R-M*, *M-T*, and *T-C* phase transition processes in sequence, which is consistent with previous work [31].

In addition to temperature, the phase transition of <001>-oriented PMN-PT single crystals is also closely related to the electric field. The phase transition induced by an electric field can usually cause a sudden change in polarization, as shown in Figure 2. In order to more accurately determine the critical electric field of the phase transition, the change rate of the unipolar polarization with the electric field, i.e.,  $dP/dE$ , is calculated at different temperatures. As shown in Figure 2, at 30 °C, there is a peak at  $E = 10.5 \text{ kV/cm}$  in the polarization curve (red line) during the process of applying an electric field, which represents the *R-M* phase transition. However, due to the hysteresis, the *M* phase re-transforms to the *R* phase in the process of withdrawing the electric field at  $E = 4.1 \text{ kV/cm}$  (green line). The electric field-induced *M-T* phase transition first appeared at 55 °C. At this time, *R-M* was induced by a lower electric field, and *M-T* was induced under a higher electric field, thus realizing that the  $dP/dE$  peaks produced by the *R-M* and *M-T* phase transitions could co-exist on the same curve. This result proves that the crystal needs to undergo *R-M* and *M-T* two-phase transitions in the process of transforming from the initial *R* phase to the *T* phase through a stable *M* phase under the multiple fields of electric field and temperature. While near the *T-C* phase transition temperature ( $T_m$  in Figure 1a), there will also be a sudden change in polarization and a  $dP/dE$  peak, indicating the *C-T* transition under the action of an electric field, as shown in Figure 2m–p.

According to the peak position of  $dP/dE$  at different temperatures, an electric field-temperature (*E-T*) phase diagram is drawn, as shown in Figure 3. Regardless of the *R-M* phase transition or the *M-T* phase transition, the phase boundary in the *E-T* phase diagram is a linear phase boundary with a negative slope. This shows that their phase transition temperature decreases linearly with the increase in the electric field, while the phase transition temperature of the *T* and *C* phases increases nonlinearly with the increase in electric field. The *T-C* phase boundary in the *E-T* phase diagram has a positive slope.

### 3.2. The Relationship between the EC Behaviors and the Phase Transitions

Figure 4a shows the bipolar polarization versus electric field (*P-E*) loops of <001> PMN-30PT single crystals measured at different temperatures. In the entire test temperature range from room temperature to 160 °C, the samples exhibit typical ferroelectric phase hysteresis loops with high squareness and high polarization with  $P_{max} > 27 \mu\text{C}/\text{cm}^2$ . The shape and value of the hysteresis loop prove that the crystal is always in the ferroelectric phase. In order to further clarify the change law of polarization with temperature, the polarization is counted under different electric fields at different temperatures, as shown in Figure 4b. Here, we take the remanent polarization ( $P_r$ ) as an example to introduce the polarization behavior of the <001> PMN-30PT single crystals. In the range of room temperature to 60 °C,  $P_r$  decreases linearly with increasing temperature. Combined with the previous research [31], it can be seen that the single crystal is a single ferroelectric *R* phase in this temperature range. While between 60 and 73 °C, the polarization increases with the increase in temperature.

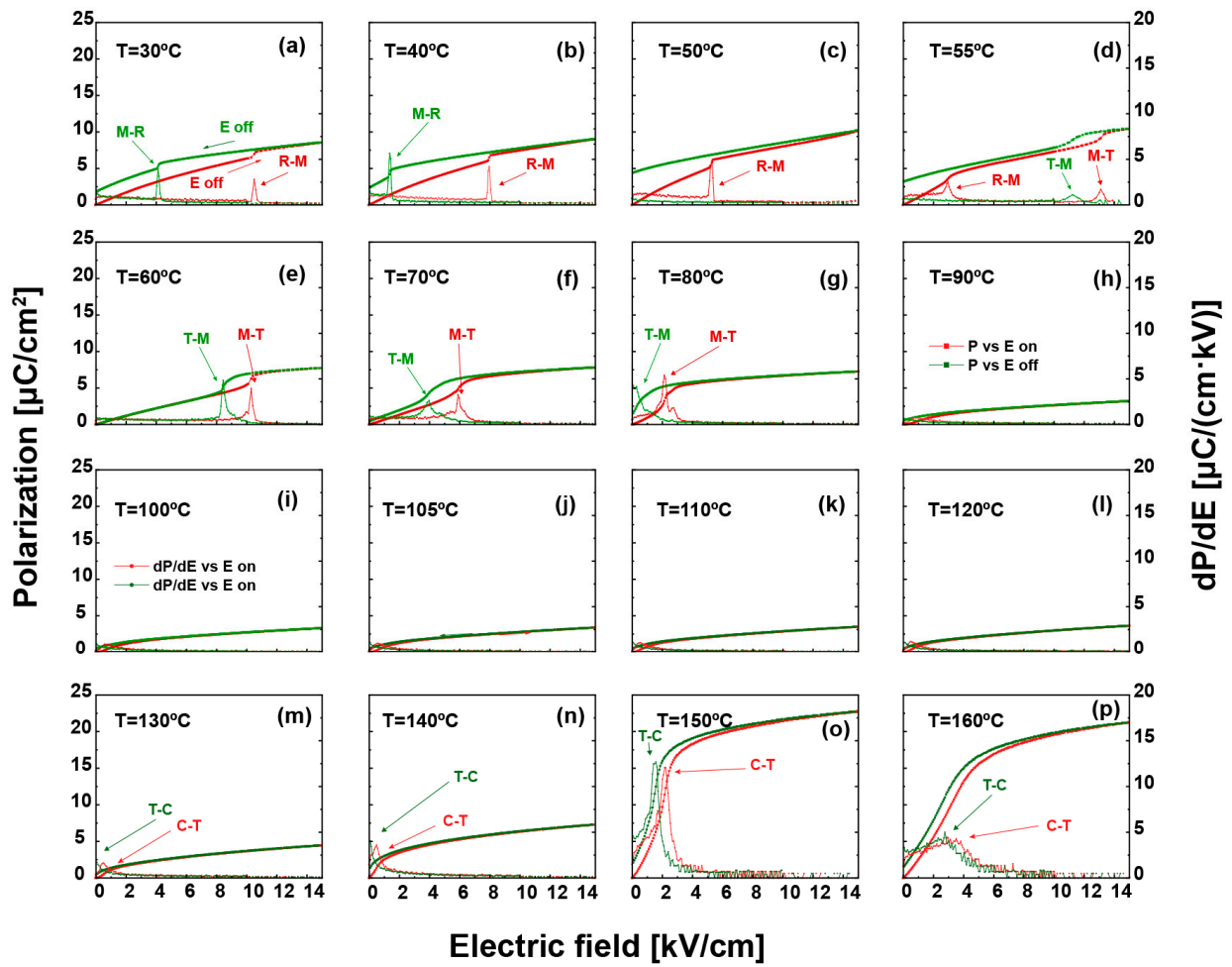


Figure 2. The polarization behavior of <001>-oriented PMN-30PT single crystals under electric field at different temperatures. (a–p) are the polarization (left axis) and polarization current (right axis) in the range of 30–160 °C, respectively.

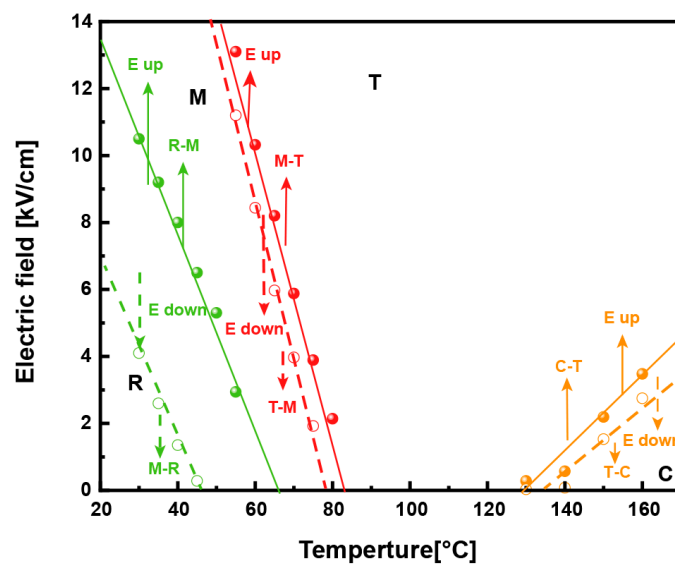
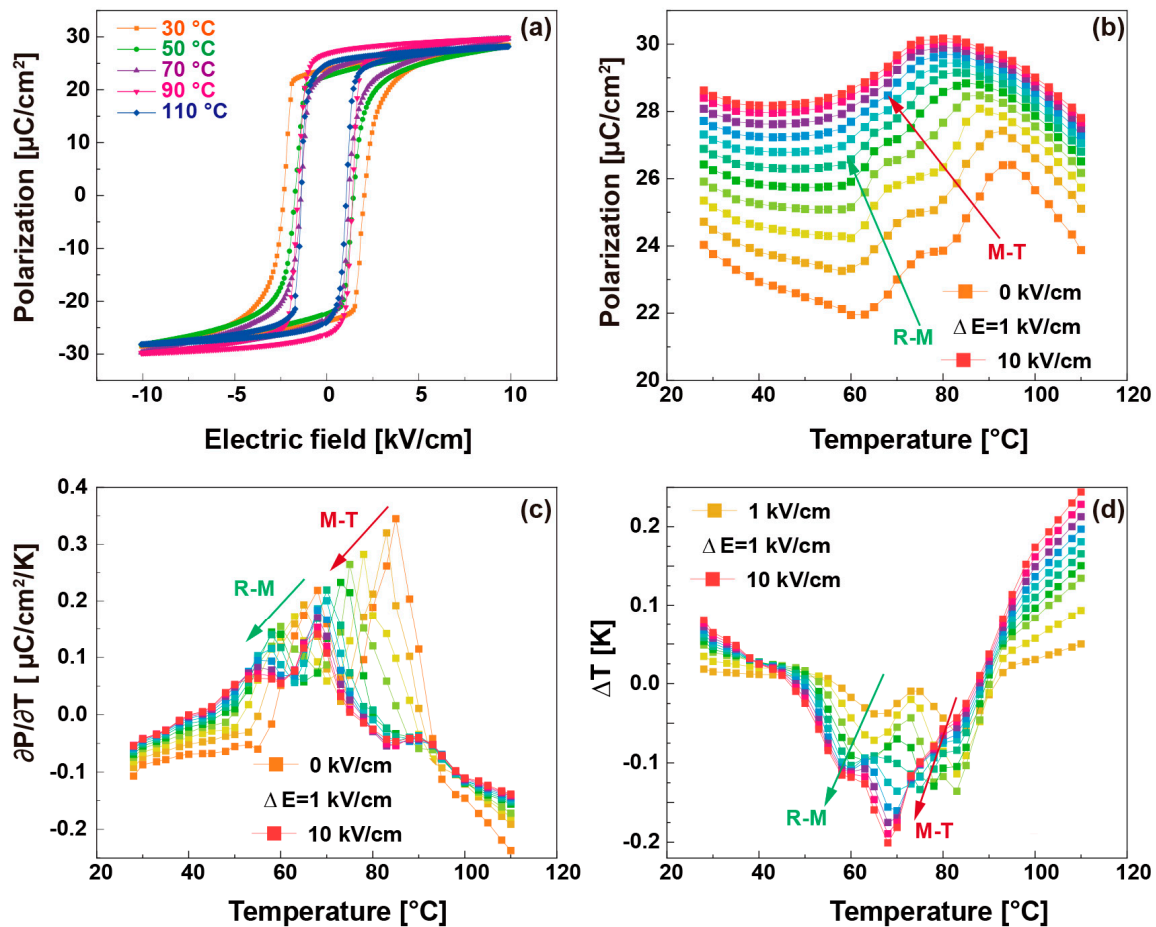


Figure 3. Electric field-temperature phase diagram of <001>-oriented PMN-30PT single crystals.



**Figure 4.** Electrocaloric effect of <001>-oriented PMN-30PT single crystals: (a)  $P$ - $E$  loops at different temperatures, the different colored lines represent different test temperatures; (b)  $P$ - $T$  curves; (c)  $(\partial P/\partial T)_E$ - $T$  curves; (d)  $\Delta T$ - $T$  curves. The different colored lines in (b–d) represent the different electric field strength from 0 to 10 kV/cm at 1 kV/cm intervals.

According to previous studies [31,32], this polarization behavior indicates the occurrence of  $R$ - $M$  phase transition induced by non-collinear electric field, which is similar to the transition from antiferroelectric ( $AFE$ ) to ferroelectric ( $FE$ ) phase in the antiferroelectric field [14] or from low-temperature ferroelectric phase to high-temperature ferroelectric phase transition induced by the non-collinear electric field in the  $BaTiO_3$  single-crystal material [13]. As the temperature further increases, the  $M$  phase tends to be stable in the late stage of the  $R$ - $M$  phase transition. Although the  $R$ - $M$  phase transition still increases the polarization, the polarization of the ferroelectric  $M$  phase decreases with increasing temperature. Under the competition of these two mechanisms, a plateau area with a narrower temperature zone of polarization is formed between 75 and 80 °C. Subsequently, the polarization ushered in another increase (80–93 °C) as the temperature continued to rise, which was induced by another phase transition, that is, the  $M$ - $T$  phase transition. When the temperature is higher than 95 °C, the polarization decreases as the temperature increases due to the depolarization of the ferroelectric  $T$  phase in the temperature field. Based on the above analysis, the evolution process from the  $R$  phase to the  $T$  phase under the temperature field can be divided into the following five parts, which are  $R$  phase,  $R$ - $M$  phase transition,  $M$  phase,  $M$ - $T$  phase transition, and  $T$  phase in succession. Among them, the depolarization of the ferroelectric  $R$ ,  $M$ , and  $T$  phases causes the polarization to decrease with increasing temperature, but the  $R$ - $M$  and  $M$ - $T$  phase transitions induce the polarization to increase.

In addition to temperature, the polarization behavior is also very dependent on the electric field. The characteristic change points of polarization all move toward lower temperatures with the increase in electric field, which are consistent with the *R-M* and *M-T* phase transitions in Figure 3. In addition, under a low electric field, the polarization plateau generated by the *M* phase can separate the increased polarization regions induced by the *R-M* and *M-T* phase transitions. But as the electric field increases, the platform becomes less and less obvious until it disappears. So when the electric field is  $E = 10$  kV/cm, the original two separate areas of increased polarization merge together. The evolution process of polarization can only be divided into three regions: polarization reduction area for the depolarization in a low-temperature *R* phase, the polarization increase area caused by phase transformation from *R* phase to *T* phase in the middle-temperature range, and polarization decrease area for the depolarization in high-temperature *T* phase.

The derivative of polarization with temperature under different electric fields, i.e., pyroelectric coefficient  $(\partial P/\partial T)_{E-T}$ , curves are calculated to study the *R-M* and *M-T* phase transitions under the action of the electric field more clearly, as shown in Figure 4c. Under each electric field, there are two positive peaks in the  $(\partial P/\partial T)_{E-T}$  curve. The low-temperature peak is induced by the *R-M* phase transition, and the high-temperature peak is induced by the *M-T* phase transition. As the electric field increases, the peaks generally move toward the low temperature, and the peak values decrease.

Generally, the decrease in the polarization with the increase in temperature can produce a positive EC effect. And on the contrary, the increase in polarization can induce a negative EC effect. Based on the thermodynamic Maxwell relation  $(\partial S/\partial E)_T = (\partial P/\partial T)_E$ , the adiabatic temperature change,  $\Delta T$  of <001>-oriented PMN-30PT single crystals are calculated using the following formula:

$$\Delta T = -\frac{T}{C\rho} \int_{E_1}^{E_2} \left( \frac{\partial P}{\partial T} \right)_E dE \quad (4)$$

where  $T$  is the sample temperature;  $C$  is the heat capacity under the electric field, which is given elsewhere [22];  $\rho$  is the density measured by Archimedes' method;  $E_1$  and  $E_2$  are the initial and final applied electric fields, respectively;  $(\partial P/\partial T)_E$  is the pyroelectric coefficient given in Figure 4c.

Figure 4d plots the complex EC behaviors of <001>-oriented PMN-30PT single crystals under the multiple fields of temperature and electric field. As the temperature rises, the  $\Delta T$  behaviors generally follow the trend of positive  $\rightarrow$  negative  $\rightarrow$  negative  $\rightarrow$  positive. Under low-temperature conditions, the positive EC effect originates from the polarization elongation in the pure *R* phase under the adiabatic condition, and its value increases as the electric field increases. When the electric field is 10 kV/cm, the value of  $\Delta T$  can reach 0.08 K at room temperature. As the temperature increases,  $\Delta T$  gradually changes from a positive value to a negative value. The first valley of  $\Delta T$  (negative EC peak) is induced by the *R-M* phase transition. The position of the valley moves to low temperature, and the value of the EC effect (the absolute value of  $\Delta T$ ) becomes larger as the electric field increases. For example, the EC effect reaches its peak value with  $\Delta T = -0.04$  K at 65 °C with  $E = 1$  kV/cm and  $\Delta T = -0.11$  K at 58 °C with  $E = 10$  kV/cm, respectively.

After the *R-M* phase transition, the negative  $\Delta T$  has decreased ( $E \leq 4$  kV/cm) due to the positive EC effect induced by the *M* phase. As the electric field strength increases, the two negative EC peaks gradually merge, which represents that the two-phase transitions of *R-M* and *M-T* (especially the *M-T* phase transition) will jointly compress the living space of the *M* phase and make the *M* phase unstable. In the previous reports using the Maxwell relation [16], there was only one negative EC peak within the test temperature range with  $\Delta E = 10$  kV/cm, which may also be the reason. As the temperature further increased, another  $\Delta T$  valley was induced by the *M-T* phase transition. Similarly, the position and value of the valley strongly depend on the magnitude of the electric field. As the electric field increases from 1 kV/cm to 10 kV/cm, the position of the valley decreases from 83 °C to 68 °C, and the value of the valley increases from  $-0.06$  K to  $-0.22$  K. After the *M-T*

phase transition, the crystal steps into the pure ferroelectric  $T$  phase, and the  $\Delta T$  turns into a positive value.

Theoretical calculations show that there are also two negative EC peaks in  $\langle 011 \rangle$ -oriented BaTiO<sub>3</sub> single crystals [13], induced by R-O phase transition near  $-90^\circ\text{C}$  and O-T phase transition near  $10^\circ\text{C}$ . Compared with  $\langle 011 \rangle$ -oriented BaTiO<sub>3</sub> single crystal, the two negative EC peaks of  $\langle 001 \rangle$ -oriented PMN-30PT single crystal are consecutive, which is conducive to expanding the temperature range of negative EC effect and making it more suitable for combining positive and negative EC effects to improve refrigeration performance.

### 3.3. EC Behaviors and Physical Mechanisms

In order to establish the relationship between the EC behaviors and physical mechanisms, the  $(\partial P/\partial T)_E$  and  $\Delta T$  are projected in the  $E$ - $T$  phase diagram, as shown in Figure 5. For the  $(\partial P/\partial T)_E$ , the first peak appears at the R-M phase boundary, and the second peak depends on the M-T phase boundary at the low electric field. Under a high electric field, the peak positions slightly deviate from the phase boundaries toward a high temperature. This is mainly because the contribution of polarization elongation in pure  $M$  phase or  $T$  phase gradually increases, driven by the high electric field. The peaks of  $\Delta T$  are also associated with the phase boundaries at low electric fields. However, as the electric field increases, the peak positions will deviate from the phase boundaries, and the deviation is even greater than that of the  $(\partial P/\partial T)_E$ . For the electric field-induced phase transition, the phase transition temperature will move toward low temperature with the increase in the electric field, so the superposition in the calculation process of the  $\Delta T$  will increase the degree of deviation at the high electric field.

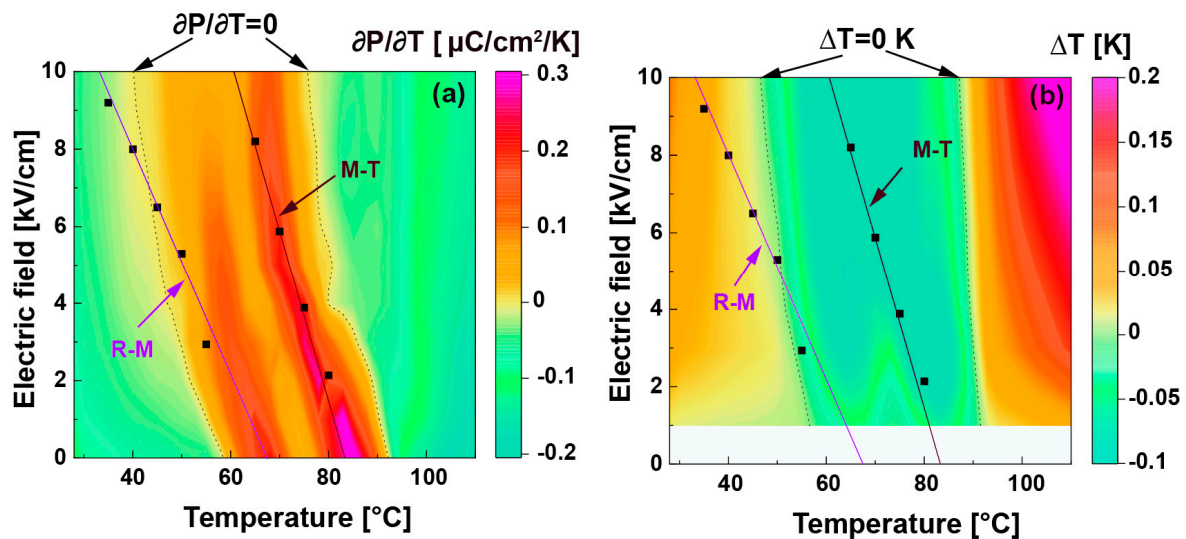


**Figure 5.** The  $(\partial P/\partial T)_E$  (a) and  $\Delta T$  (b) in the electric-temperature phase diagram of  $\langle 001 \rangle$ -oriented PMN-30PT single crystals.

According to Maxwell relation and Equation (4), the EC behaviors are the manifestations of entropy change ( $\Delta S$ ) under multiple fields of electric field and temperature [23]. Figure 6 depicts the intrinsic relationship between free energy, dipolar entropy ( $S$ ), and  $\Delta S$ , as well as the  $\Delta T$  based on the LGD potential model (1). Figure 6a shows the polarization parameter  $P_3$  along the direction of the electric field with  $E = 0$  and  $E = 1$  kV/cm. Figure 6b depicts the total free energy of PMN-30PT single crystal under different electric fields. As the temperature rises, the material changes from the initial  $R$  phase to the  $M$  phase and  $T$  phase successively and finally stabilizes to the  $C$  phase, as shown in Figures 1 and 6a, and the free energy continues to increase throughout the process. The external electric field will reduce the free energy of the material. Based on the equation  $S(E, T) = -[(\partial G_{E,T}/\partial T)]_E$  [23], the  $S$  and  $\Delta S$  were calculated, as shown in Figure 6c,d. When the crystal is in the  $R$  phase,

the  $S(E = 0, T_i) > S(E = 1, T_i)$ , which indicates that the addition of an electric field can induce a decrease in entropy ( $\Delta S < 0$ ). During the  $R$ - $M$ - $T$  phase transition stage, the electric field induces  $S$  increase ( $\Delta S > 0$ ). At the  $R$ - $M$  and  $M$ - $T$  phase transitions,  $\Delta S$  exhibits two positive peaks, as shown in the enlarged illustration in Figure 6d. Near the  $T$ - $C$  phase transitions, the electric field can induce  $S$  reduction, resulting in a distinct positive peak on the  $\Delta S$  curve.

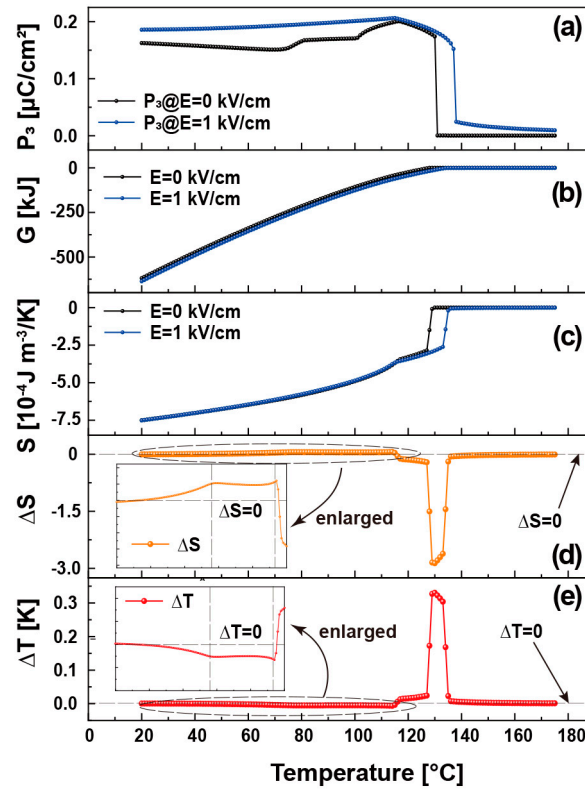


**Figure 6.** Intrinsic relationship between polarization (a), free energy (b), dipolar entropy (c), and entropy change (d) as well as the  $\Delta T$  (e) of  $\langle 001 \rangle$  oriented PMN-30PT single crystals.

Figure 6e shows the  $\Delta T$ , which is calculated as [23]

$$\Delta T = T_i \exp \left\{ -\frac{1}{C} [S(E_f, T_f) - S(E_i, T_i)] \right\} - T_i \quad (5)$$

where  $T_i$  and  $T_f$  are the temperatures. The type of EC effect (negative or positive) depends on the relationship (cooperative or antagonistic) between the temperature or electric field on  $S$ . Based on Equation (5), it is apparent that the magnitude and nature of the EC effect are contingent upon the magnitude and nature of  $\Delta S$ . In the pure ferroelectric phases,  $R$  (rhombohedral),  $M$  (monoclinic), and  $T$  (tetragonal), the rise in temperature induces an increased disorder, resulting in a marginal increase in material entropy. Conversely, the application of an electric field-induced polarization order leads to a slight reduction in material entropy. Consequently, the antagonistic relationship between temperature and electric field restricts the ferroelectric phase's ability to generate a substantial increase in entropy, thereby inducing a small positive EC effect, while the phase transition-induced  $\Delta S$  exhibits a significantly larger magnitude, resulting in a substantially greater  $\Delta T$  value than that observed in the corresponding pure ferroelectric phase. During the  $R$ - $M$  or  $M$ - $T$  phase transitions, the electric field further induces a transition from low-temperature (low-entropy) phases to high-temperature (low-entropy) phases, as depicted in Figure 3, thereby facilitating an increase in entropy. Consequently, the electric field-induced  $R$ - $M$  and  $M$ - $T$  transitions manifest as two negative EC peaks. Conversely, during the  $T$ - $C$  phase transition, the rise in temperature promotes the transformation from the  $T$  phase to the

C phase. However, the electric field stimulates the transition from the C phase to the T phase, resulting in an entropy reduction process, whereby the material dissipates heat to the environment, thus generating a positive EC peak. The magnitude of  $\Delta T$  is contingent upon the value of  $\Delta S$ . The relationship between the absolute values of  $\Delta T$  generated by the R-M, M-T, and T-C transitions follows the pattern  $|\Delta T_{T-C}| > |\Delta T_{M-T}| > |\Delta T_{R-M}|$ , as dictated by the  $|\Delta S|$  relationship.

Due to the  $\Delta S$  peak generated by phase transition, the  $\Delta T$  peak usually appears near the phase transition. Due to the participation of the electric field, the peak position usually deviates from the dielectric phase transition temperature. Near the phase transition from the low-temperature phase to the high-temperature phase, the peak temperature of the negative EC peak is usually lower than the dielectric phase transition temperature. While near the phase transition from the high-temperature phase to the low-temperature phase, the peak temperature of the positive EC peak is usually higher than the dielectric phase transition temperature.

#### 4. Conclusions

In summary, we characterized the ECE behaviors of <001>-oriented PMN-30PT single crystals under the multiple fields of electric field and temperature, and two consecutive negative ECE peaks have been found for the first time. By mapping the  $\Delta T$  onto the E-T phase diagram, the relationship between the micro mechanism and EC response is further clearly established. It was found that the two consecutive negative ECE peaks originated from the R-M and M-T phase transitions, which reach their extreme values with  $\Delta T_{max} = -0.11$  K at 57 °C and  $\Delta T_{max} = -0.22$  K at 68 °C, respectively. In addition, based on thermodynamic calculations, the relationship between the entropy behavior of each micro mechanism and the EC behavior has been depicted. The negative EC effect originates from the entropy increase in the electric-field-induced phase transition process. The entropy difference between the two phases determines the magnitude of the EC peaks. The positive or negative EC is related to the influence relationship of electric field and temperature on microstructural changes. When the electric field and temperature have the same response to the microstructure, the change in microstructure can produce a negative EC effect. If there is an opposite response, a positive EC effect will be induced. Our work provides deeper insight into the physical mechanism and corresponding EC behaviors in high-performance relaxor ferroelectric single crystal, which can promote the research progress in the related EC and piezoelectric fields.

**Author Contributions:** Writing—original draft preparation, Y.Z. and J.L.; project administration, Y.Z., W.G., Z.L. and C.L.; resources, J.C. and Y.Y.; writing—review and editing, Y.B. and W.-F.R. All authors have read and agreed to the published version of the manuscript.

**Funding:** This work was supported by grants from the Natural Science Foundation of Shandong Province (ZR2022QE078), the Basic Research Project of Qilu University of Technology (2023PX012, 2023RCKY120), and the Guangdong Provincial Key Laboratory of Electronic Functional Materials and Devices (EFMD2022013M). Young Innovative Talents Introduction and Cultivation Program for Colleges and Universities of Shandong Province (Granted by the Department of Education of Shandong Province, Sub-Title: Innovative Research Team of High-Performance Integrated Device) is also acknowledged.

**Data Availability Statement:** The original contributions presented in the study are included in the article, further inquiries can be directed to the corresponding author.

**Conflicts of Interest:** The authors declare that they have no known competing financial interests or personal relationships in this paper.

#### References

1. Grocholski, B. Cooling in a warming world. *Science* **2020**, *370*, 776–777. [[CrossRef](#)] [[PubMed](#)]
2. Shi, J.; Han, D.; Li, Z.; Yang, L.; Lu, S.-G.; Zhong, Z.; Chen, J.; Zhang, Q.M.; Qian, X. Electrocaloric cooling materials and devices for zero-global-warming-potential, high-efficiency refrigeration. *Joule* **2019**, *3*, 1200–1225. [[CrossRef](#)]

3. Kobeko, P.P.; Kurchatov, I.V. Dielectric properties of ferroelectrics. *Z. Phys.* **1930**, *66*, 192–205. [[CrossRef](#)]
4. Mischenko, A.S.; Zhang, Q.; Scott, J.F.; Whatmore, R.W.; Mathur, N.D. Giant electrocaloric effect in thin-film  $\text{PbZr}_{0.95}\text{Ti}_{0.05}\text{O}_3$ . *Science* **2006**, *311*, 1270–1271. [[CrossRef](#)] [[PubMed](#)]
5. Neese, B.; Chu, B.; Lu, S.-G.; Wang, Y.; Furman, E.; Zhang, Q.M. Large electrocaloric effect in ferroelectric polymers near room temperature. *Science* **2008**, *321*, 821–823. [[CrossRef](#)] [[PubMed](#)]
6. Zhang, S.; Deliyore-Ramírez, J.; Deng, S.; Nair, B.; Pesquera, D.; Jing, Q.; Vickers, M.E.; Crossley, S.; Ghidini, M.; Guzmán-Verri, G.G.; et al. Highly reversible extrinsic electrocaloric effects over a wide temperature range in epitaxially strained  $\text{SrTiO}_3$  films. *Nat. Mater.* **2024**, *23*, 639–647. [[CrossRef](#)]
7. Zheng, S.; Du, F.; Zheng, L.; Han, D.; Li, Q.; Shi, J.; Chen, J.; Shi, X.; Huang, H.; Luo, Y.J.S. Colossal electrocaloric effect in an interface-augmented ferroelectric polymer. *Science* **2023**, *382*, 1020–1026. [[CrossRef](#)]
8. Ma, R.; Zhang, Z.; Tong, K.; Huber, D.; Kornbluh, R.; Ju, Y.S.; Pei, Q. Highly efficient electrocaloric cooling with electrostatic actuation. *Science* **2017**, *357*, 1130–1134. [[CrossRef](#)]
9. Li, J.; Torelló, A.; Kovacova, V.; Prah, U.; Aravindhan, A.; Granzow, T.; Usui, T.; Hirose, S.; Defay, E.J.S. High cooling performance in a double-loop electrocaloric heat pump. *Science* **2023**, *382*, 801–805. [[CrossRef](#)]
10. Wang, Z.; Bo, Y.; Bai, P.; Zhang, S.; Li, G.; Wan, X.; Liu, Y.; Ma, R.; Chen, Y. Self-sustaining personal all-day thermoregulatory clothing using only sunlight. *Science* **2023**, *382*, 1291–1296. [[CrossRef](#)]
11. Qian, X.; Han, D.; Zheng, L.; Chen, J.; Tyagi, M.; Li, Q.; Du, F.; Zheng, S.; Huang, X.; Zhang, S.; et al. High-entropy polymer produces a giant electrocaloric effect at low fields. *Nature* **2021**, *600*, 664–669. [[CrossRef](#)] [[PubMed](#)]
12. Bai, Y.; Zheng, G.; Shi, S. Abnormal electrocaloric effect of  $\text{Na}_{0.5}\text{Bi}_{0.5}\text{TiO}_3$ - $\text{BaTiO}_3$  lead-free ferroelectric ceramics above room temperature. *Mater. Res. Bull.* **2011**, *46*, 1866–1869. [[CrossRef](#)]
13. Marathe, M.; Renggli, D.; Sanlialp, M.; Karabasov, M.O.; Shvartsman, V.V.; Lupascu, D.C.; Grünebohm, A.; Ederer, C. Electrocaloric effect in  $\text{BaTiO}_3$  at all three ferroelectric transitions: Anisotropy and inverse caloric effects. *Phys. Rev. B* **2017**, *96*, 14102. [[CrossRef](#)]
14. Geng, W.; Liu, Y.; Meng, X.; Bellaiche, L.; Scott, J.F.; Dkhil, B.; Jiang, A. Giant negative electrocaloric effect in antiferroelectric la-doped  $\text{Pb}(\text{ZrTi})\text{O}_3$  thin films near room temperature. *Adv. Mater.* **2015**, *27*, 3165–3169. [[CrossRef](#)] [[PubMed](#)]
15. Vales-Castro, P.; Faye, R.; Vellvehi, M.; Nouchokgwe, Y.; Perpiñà, X.; Caicedo, J.M.; Jordà, X.; Roleder, K.; Kajewski, D.; Perez-Tomas, A.; et al. Origin of large negative electrocaloric effect in antiferroelectric  $\text{PbZrO}_3$ . *Phys. Rev. B* **2021**, *103*, 054112. [[CrossRef](#)]
16. Peräntie, J.; Hagberg, J.; Uusimäki, A.; Jantunen, H. Electric-field-induced dielectric and temperature changes in a 011-oriented  $\text{Pb}(\text{Mg}_{1/3}\text{Nb}_{2/3})\text{O}_3$ - $\text{PbTiO}_3$  single crystal. *Phys. Rev. B* **2010**, *82*, 134119. [[CrossRef](#)]
17. Ma, Y.-B.; Novak, N.; Koruza, J.; Yang, T.; Albe, K.; Xu, B.-X. Enhanced electrocaloric cooling in ferroelectric single crystals by electric field reversal. *Phys. Rev. B* **2016**, *94*, 100104. [[CrossRef](#)]
18. Lu, B.; Jian, X.; Lin, X.; Yao, Y.; Tao, T.; Liang, B.; Luo, H.; Lu, S.G. Enhanced electrocaloric effect in  $0.73\text{Pb}(\text{Mg}_{1/3}\text{Nb}_{2/3})\text{O}_3$ - $0.27\text{PbTiO}_3$  single crystals via direct measurement. *Crystals* **2020**, *10*, 451. [[CrossRef](#)]
19. Wu, H.-H.; Zhu, J.; Zhang, T.-Y. Pseudo-first-order phase transition for ultrahigh positive/negative electrocaloric effects in perovskite ferroelectrics. *Nano Energy* **2015**, *16*, 419–427. [[CrossRef](#)]
20. Ponomareva, I.; Lisenkov, S. Bridging the macroscopic and atomistic descriptions of the electrocaloric effect. *Phys. Rev. Lett.* **2012**, *108*, 167604. [[CrossRef](#)]
21. Ma, X.; Chen, M.; Liu, J.M.; Wu, D.; Yang, Y. Universal inverse electrocaloric effect in perovskites. *Phys. Rev. B* **2023**, *107*, 184105. [[CrossRef](#)]
22. Li, J.; Qin, S.; Bai, Y.; Li, J.; Qiao, L. Flexible control of positive and negative electrocaloric effects under multiple fields for a giant improvement of cooling capacity. *Appl. Phys. Lett.* **2017**, *111*, 93901. [[CrossRef](#)]
23. Shan, D.; Cai, Y.; Lei, C.; Peng, J.; He, N.; Pan, K.; Liu, Y.; Li, J. Electric-field-driven coexistence of positive and negative electrocaloric effects near room temperature for high-efficiency two-stage cooling. *Appl. Phys. Lett.* **2021**, *118*, 122905. [[CrossRef](#)]
24. Dou, J.; Li, J.; Li, J.; Zhang, H.; Yang, Y.; Bai, Y.; Rao, W.-F. Simultaneous enhancement of the electrocaloric effect and electrostrain via exploiting the reversible polarization rotation. *Ceram. Int.* **2023**, *49*, 7094–7098. [[CrossRef](#)]
25. Goupil, F.L.; Berenov, A.; Axelsson, A.-K.; Valant, M.; Alford, N.M. Direct and indirect electrocaloric measurements on  $\langle 001 \rangle$ - $\text{PbMg}_{1/3}\text{Nb}_{2/3}\text{O}_3$ - $30\text{PbTiO}_3$  single crystals. *J Appl. Phys.* **2012**, *111*, 124109.
26. Fu, H.; Cohen, R.E.J.N. Polarization rotation mechanism for ultrahigh electromechanical response in single-crystal piezoelectrics. *Nature* **2000**, *403*, 281–283. [[CrossRef](#)]
27. Katzke, H.; Dietze, M.; Lahmar, A.; Es-Souni, M.; Neumann, N.; Lee, S.G. Dielectric, ultraviolet/visible, and Raman spectroscopic investigations of the phase transition sequence in  $0.71\text{Pb}(\text{Mg}_{1/3}\text{Nb}_{2/3})\text{O}_3$ - $0.29\text{PbTiO}_3$  crystals. *Phys. Rev. B* **2011**, *83*, 174115. [[CrossRef](#)]
28. Cui, A.; Ye, Y.; Dai, K.; Li, Y.; Zhu, L.; Jiang, K.; Shang, L.; Xu, G.; Hu, Z.; Zhang, S.; et al. Designing monoclinic heterophase coexistence for the enhanced piezoelectric performance in ternary lead-based relaxor ferroelectrics. *ACS Appl. Mater. Inter.* **2022**, *14*, 10535–10545. [[CrossRef](#)]
29. Li, J.; Li, J.; Wu, H.-H.; Zhou, O.; Chen, J.; Lookman, T.; Su, Y.; Qiao, L.; Bai, Y. Influence of phase transitions on electrostrictive and piezoelectric characteristics in PMN-30PT single crystals. *ACS Appl. Mater. Inter.* **2021**, *13*, 38467–38476. [[CrossRef](#)]
30. Wu, H.H.; Cohen, R.E. Electric-field-induced phase transition and electrocaloric effect in PMN-PT. *Phys. Rev. B* **2017**, *96*, 54116. [[CrossRef](#)]

31. Li, J.; Yin, R.; Su, X.; Wu, H.-H.; Li, J.; Qin, S.; Sun, S.; Chen, J.; Su, Y.; Qiao, L.; et al. Complex phase transitions and associated electrocaloric effects in different oriented PMN-30PT single crystals under multi-fields of electric field and temperature. *Acta Mater.* **2020**, *182*, 250–256. [[CrossRef](#)]
32. Kim, I.H.; Kim, I.H.; Im, S.G.; Jang, K.O. A phenomenological study on temperature-concentration-electric field phase diagram of relaxor ferroelectrics PMN-PT single crystals. *Physica B* **2022**, *639*, 413961. [[CrossRef](#)]

**Disclaimer/Publisher’s Note:** The statements, opinions and data contained in all publications are solely those of the individual author(s) and contributor(s) and not of MDPI and/or the editor(s). MDPI and/or the editor(s) disclaim responsibility for any injury to people or property resulting from any ideas, methods, instructions or products referred to in the content.